Check for updates

ADVANCED MATERIALS TECHNOLOGIES
www.advmattechnol.de

Hybrid Manufacturing of 3D Hierarchical Porous Carbons for Electrochemical Storage

Panfeng Wang, Hao Zhang, Huizhi Wang, Dawei Li, Jin Xuan,* and Li Zhang**

Carbon is one of the most attractive electrode materials for electrochemical energy storage. An ideal electrode structure requires a pore distribution ranging from nanoscale to milliscale to simultaneously enable efficient mass transfer, enlarge the specific surface area, and minimize the electrical resistance. Here, a novel hybrid method to fabricate carbon electrodes with a designable hierarchical pore structure is presented. The proposed manufacturing combines stereolithography, pyrolysis, and chemical activation, which contribute to producing pores in millimeter, micrometer, and nanometer, respectively. The prepared hierarchical microarchitectural material outperforms the commercial carbon paper by five times in current density. Further enhancement in the electrochemical performance can be achieved through optimizing the distribution of hierarchical pores, which is proved feasible in the applications of vanadium redox flow battery and supercapacitor applications.

1. Introduction

Carbon is widely used in electrodes as both active materials and supports for the electrochemical energy storage (EES) applications,[1–3] for example, fuel cells,[4] batteries,[5] flow batteries,[6] and super-capacitors,[7] due to its superior properties such as chemical stability, environmental friendliness, and excellent electrical conductivity.[8,9] An ideal carbon electrode must present multiple functions simultaneously, such as offering fast mass diffusion routes supplying large reaction surfaces, providing rapid electrons transfer pathways, and maintaining stable reaction conditions.[8,10–12] Developing electrodes with hierarchically distributed pores at multiple length scales from nanometer to millimeter is a promising approach to achieve these desirable requirements. For example, the pores at micrometer scales can effectively guide the bulk flow of the electrolyte throughout the electrode.[13,14] Down to the microscopic level, the macropores (>50 nm) distribute the electrolyte into the inner electrode matrix and buffer the ions.[7] The mesopores between 2 and 50 nm enable efficient transport of species. The micropores under 2 nm provide tremendous electroactive sites for the electrochemical reaction.[7,10,15] The microscopic porous structures also affect the electrode resistance and electrode/electrolyte interface length.[16,17] Excellent electrical properties like large specific capacitances,[8,18] good electrocatalysis performances,[11,19] fast ion diffusivity,[8,16] and high electro-conductivity[20] can be achieved through introducing proper hierarchical structures.

Many methods have been reported to synthesis the hierarchical porous carbon structures, such as template methods,[18,21,22] aerogel,[10] direct carbonization,[23,24] and activation methods (chemical, physical,[8] hydrothermal, and molten salt[25] approach). Most of the existing protocols and synthesis methods focus on the optimization of micro- and mesostructures.[7,18] However, the importance of macro-architectures at the micrometer scale, which is crucial for the electrolyte transport,[6,26] electrode electric resistance,[27] and electrode–electrolyte interface area,[12] has been largely overlooked.

Recently, opportunities have been provided by additive manufacturing (AM) to customize macro-architectures at the micrometer scales. Several attempts were reported for the 3D printing of carbon materials, such as direct ink writing,[28,29] fused deposition modeling,[30,31] inkjet printing,[32] and select laser sintering.[33] Very recently, two-photon polymerization (2PP),[34] stereolithography (SLA),[35] and digital light processing[36] were used to print carbon materials.[37,38] Among them, the optical-based methods (2PP and SLA) present the highest printing accuracy (sub-micrometer for 2PP[34]) and minimum design limitations in model shaping, which makes the bespoke design of sophisticated porous macro-architectures possible. However, these methods are not yet ready for the manufacturing of electrode materials for EES applications due to the lack of structural control at nanoscale.

To address the gap, in this study, designable microstructure and macro-architectures were bridged by a novel hybrid process

P. Wang, Dr. D. Li, Prof. L. Zhang
School of Mechanical and Power Engineering
East China University of Science and Technology
Shanghai 200237, China
E-mail: lzhang@ecust.edu.cn
Dr. H. Zhang, Prof. J. Xuan
Department of Chemical Engineering
Loughborough University
Loughborough LE11 3TU, UK
E-mail: j.xuan@lboro.ac.uk
Dr. H. Wang
Department of Mechanical Engineering
Imperial College London
London SW7 2BU, UK
E-mail: huizhi.wang@imperial.ac.uk
The ORCID identification number(s) for the author(s) of this article can be found under https://doi.org/10.1002/admt.201901030.

© 2020 The Authors. Published by WILEY-VCH Verlag GmbH & Co. KGaA, Weinheim. This is an open access article under the terms of the Creative Commons Attribution License, which permits use, distribution and reproduction in any medium, provided the original work is properly cited.

DOI: 10.1002/admt.201901030

that couples SLA 3D printing and chemical activation. The precise SLA printing creates sophisticated macro-architectures with model-based design, followed by a well-controlled pyrolysis scheme that carbonizes the polymer structure while maintaining the design shape. A proper activation process is developed to enrich the hierarchical micro-, meso-, and macropore structures. The as-prepared 3D hierarchical porous carbon electrodes show superior performance in energy storage applications such as supercapacitor and redox flow battery.

2. Results and Discussion

2.1. Hybrid Manufacturing of Multiscale Structured Carbons

A novel hybrid approach that combines SLA and chemical activation is employed to fabricate porous carbon electrodes with tailorable hierarchical structures and compositions. As illustrated in **Figure 1**a, a 3D geometry model that defines the shape and size of the macro-architectures is first printed by SLA (Figure 1b) from the photosensitive resin (SOMOS IMAGINE 8000, DSM, Holland) as the polymer precursor. The 3D printed structure is then carbonized (Figure 1c) through well-defined slow pyrolysis. To prevent the deformation and collapse of printed structures caused by the volume shrinkage, a slow heating rate of 0.05 °C min^{-1} at the main mass loss region was chosen for the pyrolysis process. The slow heating up is found to be an effective way to release the stresses and thus help retain the designed pore shapes. A uniform shrinkage of 67.6% in dimension was measured after pyrolysis due to the stripping of non-carbon elements (Figure 1e–g), but no obvious structure deformation is spotted. Then, the activation process (Figure 1d) is conducted, during which no apparent shrinkage is detected. The scanning electron microscopy (SEM) images of the resulting activated carbons in Figure 1h clearly show the designed macro-architectures. The enlarged features (Figure 1i) show that the structure wall is covered with macropores after activation which is composed of intrinsic mesopores (Figure 1j) and micropores (Figure 1k). The other designed structures and non-carbon elements releasing pores in carbonization are presented in Figure S1, Supporting Information.

2.2. Tuning of Microscopic Pore Structures

At the microscopic level, the micropores provide high surface area for the active sites, while the mesopores enhance the active species transferring in the electrodes of EES devices.[15] Therefore, it is essential to optimize the pore size distribution to obtain an optimized structure. The pore size and distribution in the carbon matrix can be tuned by the duration, temperature, and potassium hydroxide amount in the activation process.[20,39] In this research, various mass ratios of KOH to carbon material were employed to form different porosities of the structure.

To investigate the influences of the pore distribution on the electrochemical performance, activated carbon electrode samples with different pore distribution features were tested in two typical EES applications, that is, supercapacitor and vanadium redox flow battery. The 860-Act sample is carbonized at 860 °C and activated by the KOH retained on the electrode surface after immersed in 6 M KOH at a mass ratio of 1:4. The 960-Act sample is carbonized at 960 °C and activated at a mass ratio of 6:1 (960-Act). The pore volume and BET surface of 960-Act are 0.206 cm^3 g^{-1} and 101.323 m^2 g^{-1}, respectively, both of which are larger than the values of the 860-Act, 0.018 cm^3 g^{-1} and 8.250 m^2 g^{-1}, respectively. Type I isotherm, according to IUPAC classification, are obtained for both samples (**Figure 2**a) corresponding to microporous materials.[15] The steep increase at a low relative pressure ($P/P_o < 0.05$) indicates the abundance of micropores, while the small rise at 0.5–0.9 P/P_o reveals the presence of mesopores for the 960-Act sample. The results show that 960-Act samples have more micro and mesopores than 860-Act, which is consistent with the BET analyses. The porous features are further confirmed by the pore size distribution curves,

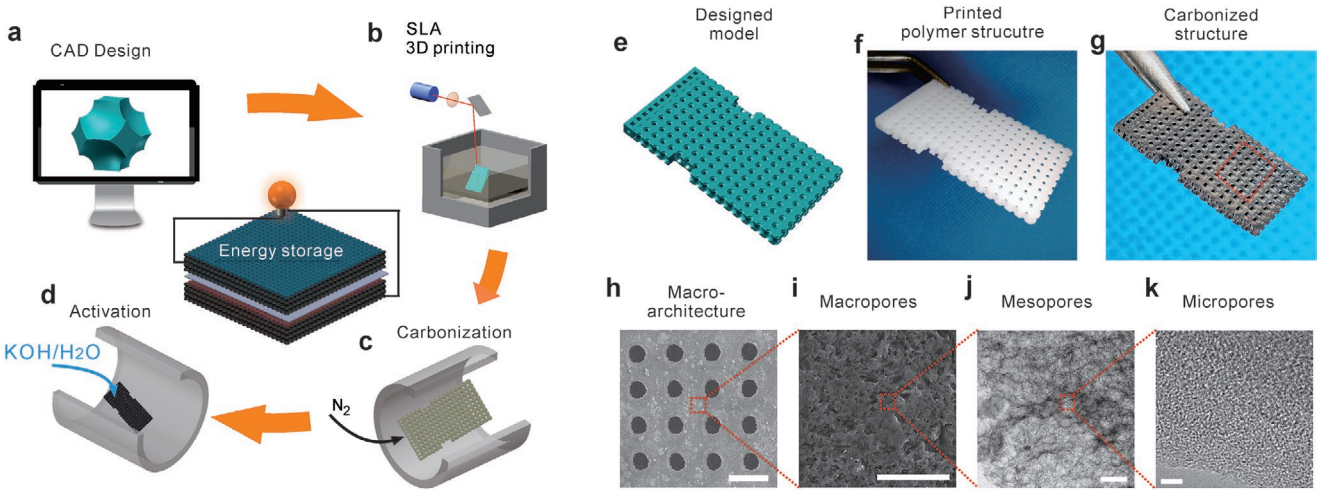


Figure 1. The proposed hybrid manufacture process of the hierarchical porous electrode. a) CAD design of the electrode with spherical and cubic pores (S25 sample); b) SLA 3D printing process; c) carbonizing process; and d) activating process. The photographs of e) CAD design of the porous electrode; f) printed porous polymer structures; and g) the carbonized carbon electrode. Electron microscopic images of the printed carbon electrode samples: h) SEM image of the macro-architectures after the activation; i) SEM image of the wall surface of the activated electrode; j,k) TEM images of the activation carbon material; scale bars: 1 mm (h); 20 µm (i); 100 nm (j); 5 nm (k).

© 2020 The Authors. Published by WILEY-VCH Verlag GmbH & Co. KGaA, Weinheim

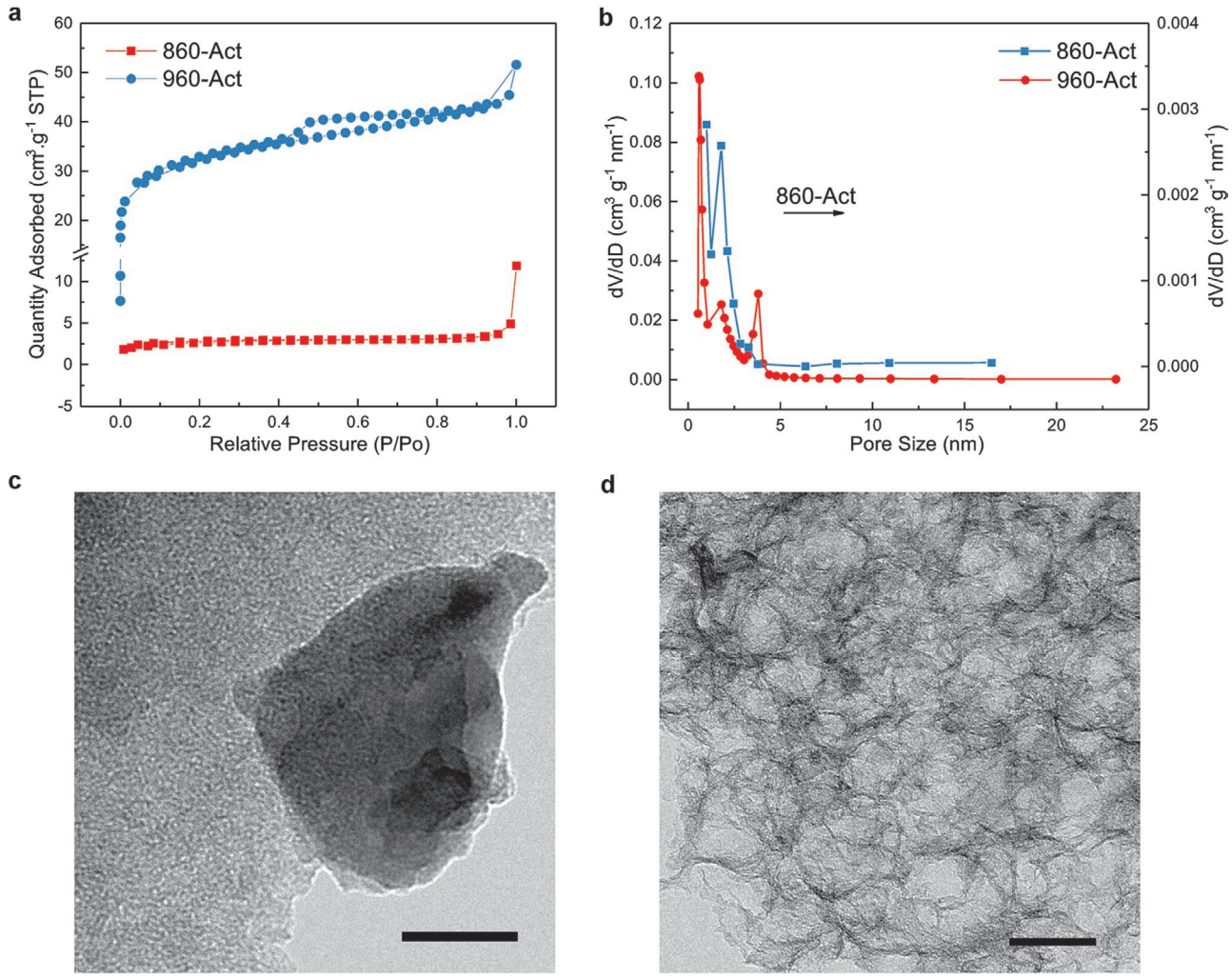


Figure 2. The mesopores and micropores of the prepared materials. a) Nitrogen adsorption–desorption isotherm; b) pore size distributions of the activation carbon; TEM images of c) 860-Act and d) 960-Act carbon. Scale bars: 50 nm.

as shown in Figure 2b. The curve of 960-Act shows two obvious peaks in the region less than 2 and at 3.8 nm, corresponding to micropores and mesopores, while the plots of 860-Act carbon only show micropores at 1.8 nm. The TEM images further confirm these phenomena. Figure 2c presents the micropore features of the 860-act carbon, and Figure 2d confirms the existence of mesopores (≈20 nm) in the 960-Act carbon.

2.3. Analysis of Prepared Materials

As shown in **Figure 3**a, the carbon yield (beyond 670 °C) is ≈1.12% in the thermogravimetric analysis (TGA) at a heating rate of 5 °C min^{-1} in the high purity nitrogen atmosphere. The initial and terminal pyrolysis temperature of the printed sample polymer precursor is about 300 and 480 °C, which is in accordance with the results of other polymer precursors.[40–43] Considering the change of the heating rate (from 0.05 to 0.5 °C min^{-1} compared with 5 °C min^{-1} at TGA) to carbonize the electrode, a broad region from 300 to 480 °C, beyond which the mass loss rate is approaching to 0, is set as main mass loss regions. After several trials at various heating rates (Figure S1d–f, Supporting Information), a much smaller heating rate (0.05 °C min^{-1}) is selected to maintain the designed shape in the carbonization. However, from the process economic aspect, the long processing time led by the slow heating rate could potentially increase the cost of the fabrication.

The energy dispersive X-ray spectroscopy (EDS) results (Figure 3b) show that the elements in the prepared materials are mainly C and O, and a handful of residual Si (Table S1, Supporting Information). The X-ray-diffraction (XRD) spectroscopy in Figure 3c displays two XRD peaks centered at ≈25° and ≈44° which can be attributed to the (002) and (100) crystallographic plane of graphite, respectively. The broad reflections peaks indicate that amorphous carbons[44,45] are obtained when the carbonization temperatures are above 760 °C. The high carbonization temperature leads to a similar crystallinity of carbon particles, but the purity of nanostructure is improved, according to the TGA and EDS analysis. Two peaks were observed in the Raman spectra (Figure 3d) for each sample at 1350 and 1590 cm^{-1}, which are corresponding to the D-band (vibration of dangling bond carbon atoms) and G-band (vibration of sp^2-bonded

© 2020 The Authors. Published by WILEY-VCH Verlag GmbH & Co. KGaA, Weinheim

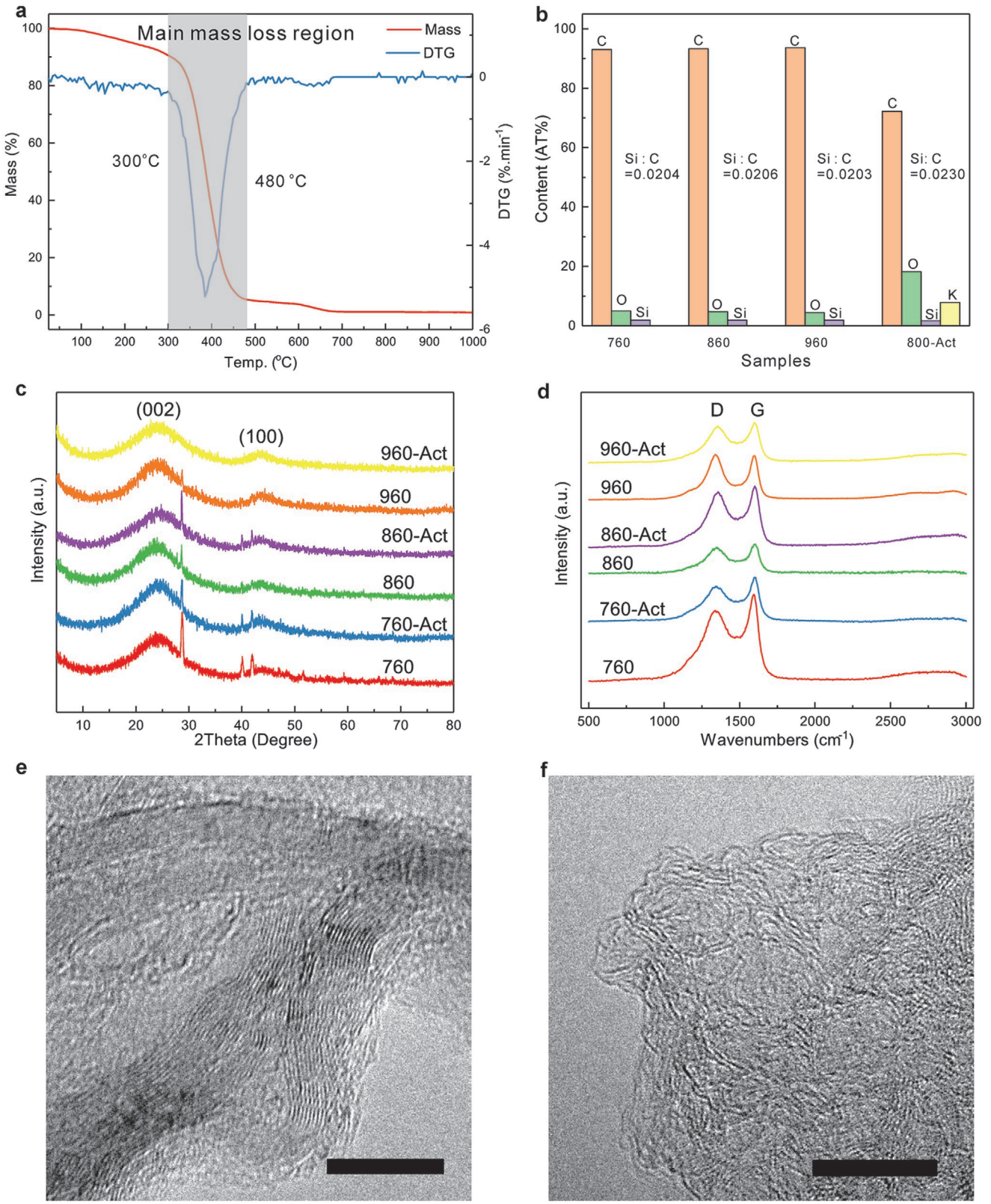


Figure 3. The materials analysis of the prepared electrodes. a) thermogravimetric analysis (TGA) and differential thermal gravity (DTG) curves of the printed resin in nitrogen atmosphere (heating rate: 5 °C min^{-1}); b) elements in the electrodes carbonized at 760, 860, and 960 °C and the sample KOH activated (3:1) at 800 °C; c) XRD pattern and d) Raman spectra of carbonized samples with and without activation; high-magnification TEM images of e) 860-Act and f) 960-Act carbon samples. Scale bars: 10 nm.

© 2020 The Authors. Published by WILEY-VCH Verlag GmbH & Co. KGaA, Weinheim

carbon atom) associated with disordered carbon and graphitic carbon, respectively.[46] The intensity ratio of D-band to G-band (I_D/I_G) can be calculated to be 0.82 to 1.03 (Table S2, Supporting Information), suggesting a highly disordered structure of the prepared carbons.[7,47] The intensity ratio differences might be ascribed to the chemical structure of the photosensitive resin precursor.[42,48]

After activation, the atom ratio of silicon to carbon is slightly increased to 0.023 from 0.0203, as shown in Figure 3b, due to the etch of the carbon by KOH in the activation process. The XRD plots (Figure 3c) and Raman spectra (Figure 3c) show that the compositions of the carbon after activation (760-Act, 860-Act) are rarely different from the corresponding non-activation samples. The distinguished decrease of the I_D/I_G of 960-Act sample compared with the 960 sample is because the KOH amount is large, which enhances the graphitization.[7,49]

The TEM images of 860-Act (Figure 3e; Figure S2, Supporting Information) and 960-Act (Figure 3f; Figure S3, Supporting Information) show the presence of the graphite with a disordered structure. Therefore, the activation process can tune the crystalline structures of carbon. In contrast, the carbonization temperature below 960 °C cannot tune the crystalline structures substantially, but the high carbonization temperature can improve the purity.

2.4. Effects of Activation Process on Electrochemical Performance

Figure 4a,b compares the electrochemical performance of a carbonized sample (C10) with and without the activation process in a classic ferri/ferro system. The electrochemical

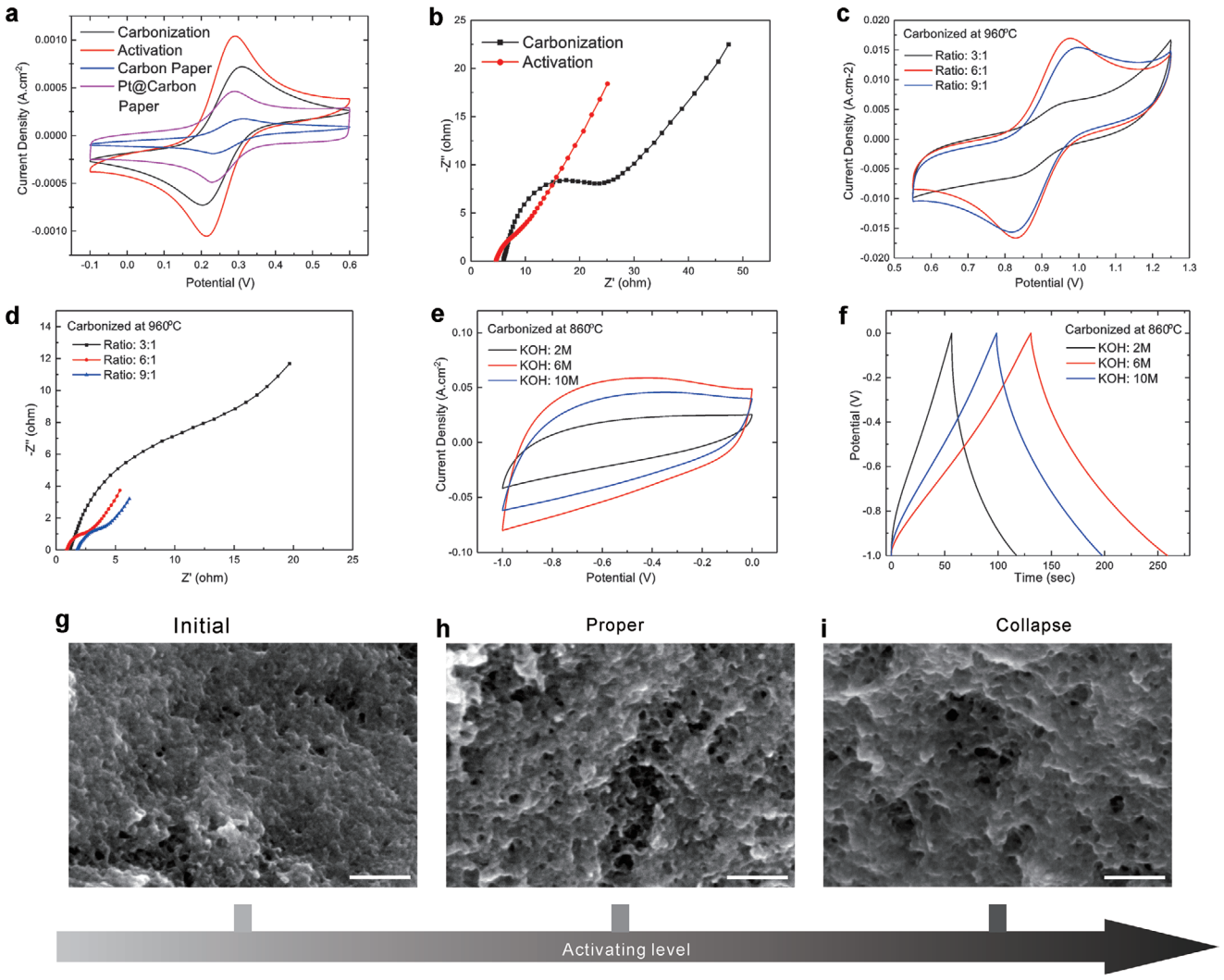


Figure 4. The electrochemical performance related with the activation conditions. a) CV curves (50 mV s^{-1}) of the water activated electrode, carbonized electrode, carbon paper, and platinum carbon paper (0.2 mg cm^{-2}); b) Nyquist plots of carbon electrodes with and without water vapor activation in 1 mM $K_3Fe(CN)_6$ + 0.5 M KCl electrolyte; c) CV curves at 10 mV s^{-1} and d) Nyquist plots curves of the KOH activated carbon electrodes in $VOSO_4$ (0.1 M) and H_2SO_4 (3 M) electrolyte; e) CV at 50 mV s^{-1} scan rate and f) galvanostatic charge–discharge curves (0.1 A g^{-1}) of the KOH activated carbon electrodes in KOH solution (6 M); the preparation conditions of these electrode is presented in Table S3 and Supporting Methods, Supporting Information; g–i) FESEM images of the carbon activated by KOH with weight ratios of 3:1, 6:1, and 9:1. Scale bars: 100 nm.

© 2020 The Authors. Published by WILEY-VCH Verlag GmbH & Co. KGaA, Weinheim

performance of commercial carbon papers (with or without Pt loading) is also presented for comparison. The activated 3D carbon material shows a 5.85-fold higher peak current density (PCD) in the cyclic voltammogram (CV) compared with carbon papers, and even higher than that of carbon paper loaded with Pt, as shown in Figure 4a. It is observed that the activation process can lower the peak-to-peak separation (ΔE_p) of the carbon electrodes, resulting in an improvement in electrocatalytic ability. The activated carbon material exhibits a ΔE_p of 75 mV, which is between the values of carbon papers without (82 mV) and with (63 mV) Pt loading. The electrochemical impedance spectroscopy (EIS) measurements in Figure 4b further confirm that the activation process can decrease both the ohmic resistance and charge transfer resistance of our carbon electrodes. The enhancement of the electrochemical performance may be attributed to the exposed edge carbon sites acting as active sites and the increase of surface area.[17,20]

The effects of activation conditions on electrochemical performance are further examined, as shown in Figure 4c–f. Figure 4c,d illustrates the CV and EIS plots of the carbon materials activated at different KOH to carbon mass ratios. It is found that PCD increases significantly with mass ratio growing from 3:1 to 6:1, while a slight drop occurs as mass ratio further rising to 9:1. The improvement of the electrochemical performance is attributed to the increase of the surface area and exposed active sites.[50,51] However, further activation results in the collapse of the activated pores, which lead to the decrease of the surface area and conductivity (Figure 4d).[51] A similar effect of the concentration of the activation agent on the electrochemical performance is found, as shown in Figure 4e,f.

The pore size evolution during the activation process is explained through field emission scanning electron microscopy (FESEM) images in Figure 4g–i. The activation is initiated at the defects and forming small pores (Figure 4g) acting as active sites.[39,52,53] The amount and the size of small pores are enlarged (Figure 4h) by further activation to achieve the desired electroactivity.[54,55] After reaching the optimal point, undesired collapse (Figure 4i) of pore structure occurs and causes loss in catalytic performance.[20,56]

2.5. Designability of Macro-Architectures through 3D Printing

The morphology, pore distribution, and size of macro-architectures in the electrode impose significant impacts on electrochemistry performance through determining the mass transfer of reactive species.[10,57,58] Here, we define the geometry of the macro-architectures by two factors, that is, the diameter of the pores and the overlap ratio (**Figure 5**a). For the pores stacked shown in Figure 5b, the overlap ratio is defined as:

$$k = (D - S) \times D^{-1};\ k \in (0, 0.29) \quad (1)$$

where k refers to the overlap ratio, D is the pore diameter, and S refers to the space between two adjacent pores, as shown in Figure 5a.

To derive a general design principle for macro-architecture morphology, electrodes with tunable micrometer holes were investigated numerically and experimentally in four aspects, that is, porosity, thickness of pore wall, specific surface area, and electrical resistance.

High porosity is regarded as favorable for mass distribution within the porous material.[15,59,60] The theoretical porosity of the porous architectures can be calculated by Equations (S8)–(S13), Supporting Information. It is found that the porosity of the structure is solely dependent on the value of overlap ratio k. As shown in Figure 5c, the porosity ranges from 0.54 to 0.96 when k grows from 0% to 29%, which matches the porosity evaluations of the geometry model derived by CAD software.

As shown in Figure 5d, the effective diffusivities of ions[61] increase for nearly four times with the growth of overlap ratio and the reciprocal of the wall thickness. The thickness of the wall between two pores is tunable through manipulating k and pore size, as indicated in Equation (S14), Supporting Information. It is found that the wall thickness decreases with the rising of overlap ratio k, while increase with the growth of pore size, as shown in Figure S4a, Supporting Information.

To accelerate the electrochemical reaction rate at the electrode, a larger specific surface area (SSA) is preferred in designing the porous structure. The SSA can be theoretically evaluated from Equations (S15)–(S20), Supporting Information. Figure 5e shows that the calculated SSA decreases with the rising of pore diameter and overlap ratio. The electrochemical active area and PCD follow the same trends as SSA along with the pore diameter and overlap ratio variations (Figure 5f), which confirms the theoretical prediction of SSA.

Keeping the electrical resistance of electrode as lower as possible is another important criterion in designing the porous structure. The electrical resistance of the ordered porous layer can be estimated by Equations (S21)–(S25), Supporting Information, which shows the resistance is affected only by overlap ratios. Figure 5g shows that the calculated resistance monotonically increases with the overlap ratio (also shown in Figure S4b, Supporting Information). The simulation results of resistance obtained from COMSOL are very close to the calculated ones. The actual ohmic resistance, which was measured by EIS (shown in Figure S5, Supporting Information), shows the same variation trend along with the overlap ratio. The current density distributions derived from COMSOL simulation within the macro-architectures are revealed in Figure 5h. It is found that the current density decreases with the overlap ratio increasing, corresponding to a resistance rising.

2.6. Electrochemical Storage Applications

The electrodes made of the bespoke carbon structures were tested in two typical electrochemical storage devices, that is, a supercapacitor (**Figure 6**a) and vanadium redox flow battery (VRFB) (**Figure 7**a).

For the case of supercapacitor, as illustrated in Figure 6a, the cation (K^+ in this test) and anion are electro-adsorbed to the corresponding electrode surface, which is oppositely charged in the charging process.[16] The performance measurements of the S00 series (Table S3, Supporting Information) samples as supercapacitor electrodes in KOH solution (6 M) are shown in Figure 6b–e. The current densities (Figure 6b) are stepping down with the designed pore diameter in the macro-architecture

© 2020 The Authors. Published by WILEY-VCH Verlag GmbH & Co. KGaA, Weinheim

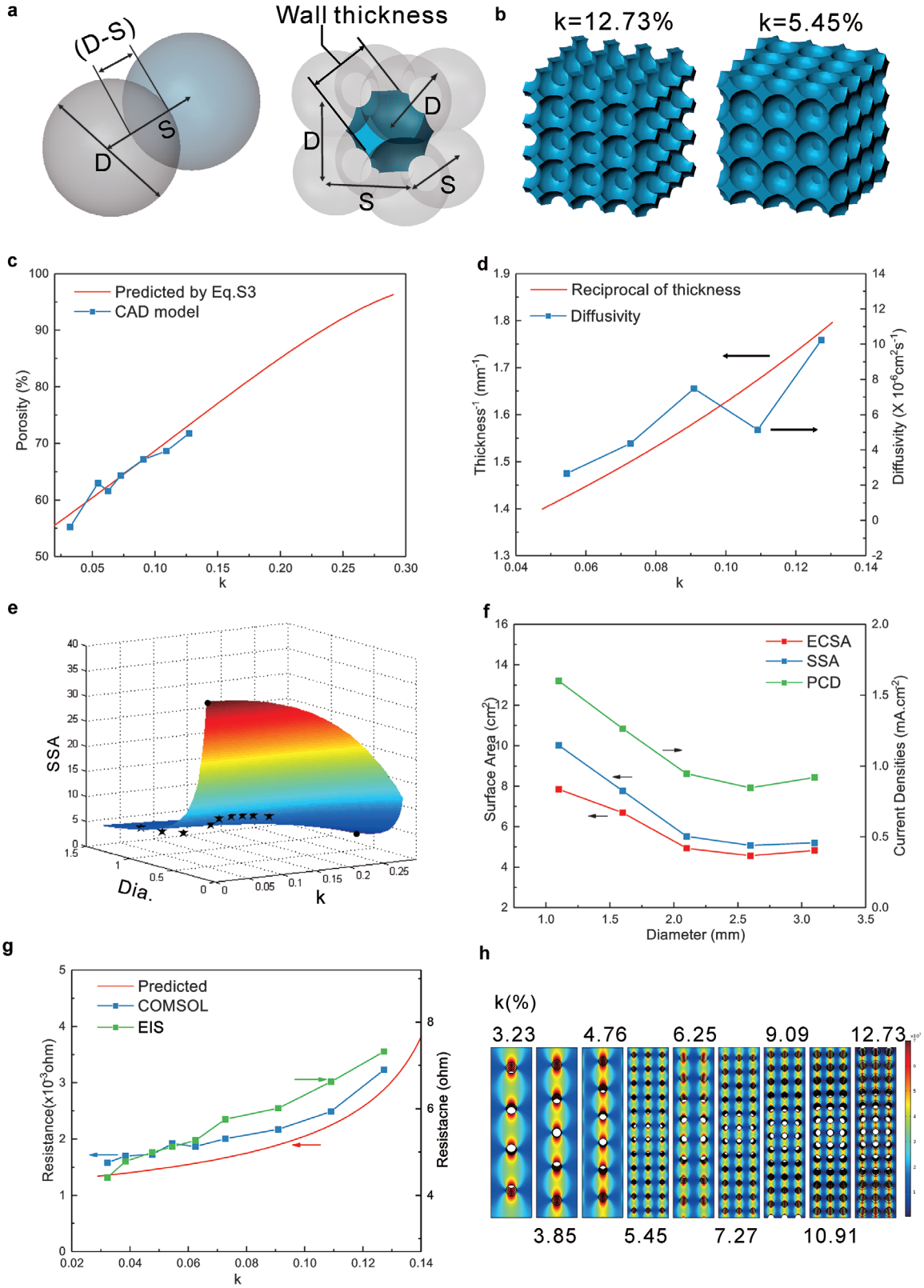


Figure 5. The structure-performance of the prepared carbon electrodes. a) The diameter, space, and overlap length; b) the pore stacking form at different overlap ratio; c) the porosity varying with overlap ratio; d) mass transport ability related to reciprocal of wall thickness; e) the SSA associated with diameter and overlap ratio; f) the electrocatalytic performance and SSA of the electrode with different diameters and *k*; g) the resistance varies with overlap ratio; h) the current densities distribution in the various electrodes simulated and visualized by COMSOL (See value on Table S4, Supporting Information).

© 2020 The Authors. Published by WILEY-VCH Verlag GmbH & Co. KGaA, Weinheim

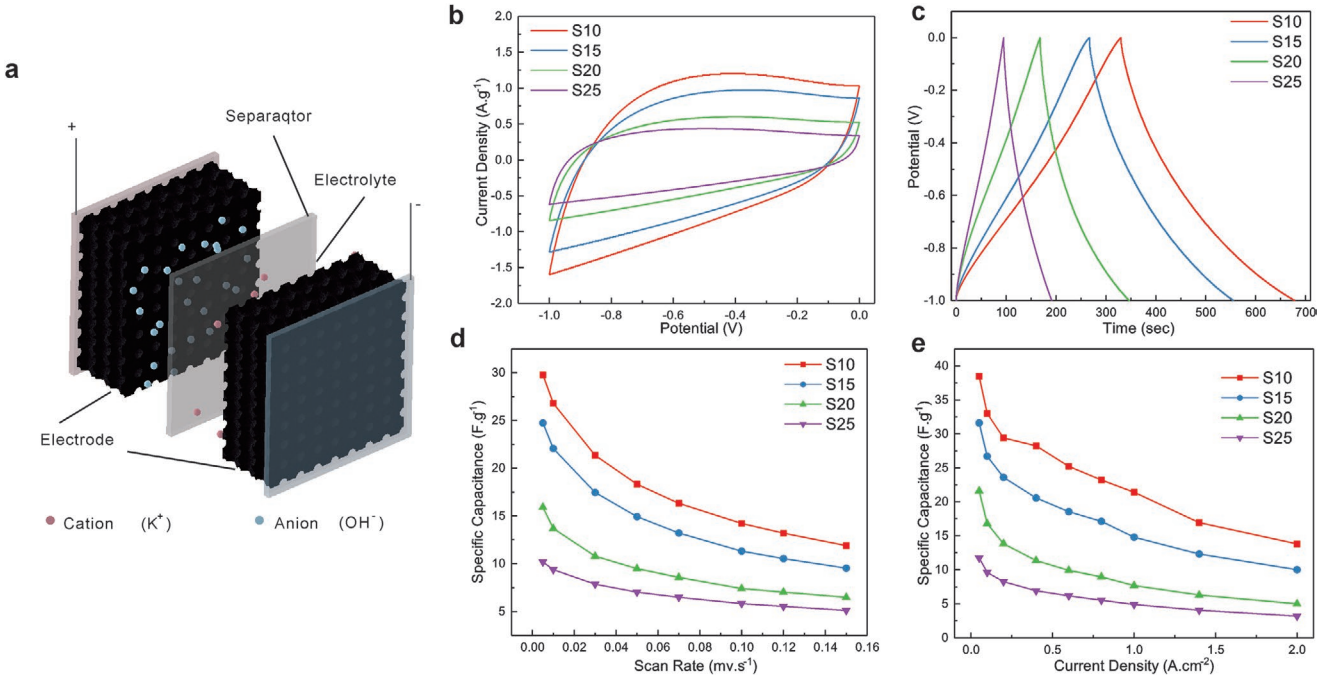


Figure 6. The printed structures used as supercapacitor electrodes. a) Schematic diagram of supercapacitor representing the static EES system; b) CV curves of electrodes with different pore diameters in KOH solution (6 M) at 50 mV s^{-1}; c) galvanostatic charge–discharge curves under 50 mA g^{-1}; d) specific capacitance of the electrodes with 1.0, 1.5, 2.0, and 2.5 mm diameter (S00 series electrodes) at various scan rates; e) specific capacitance of S00 series electrodes at different current densities.

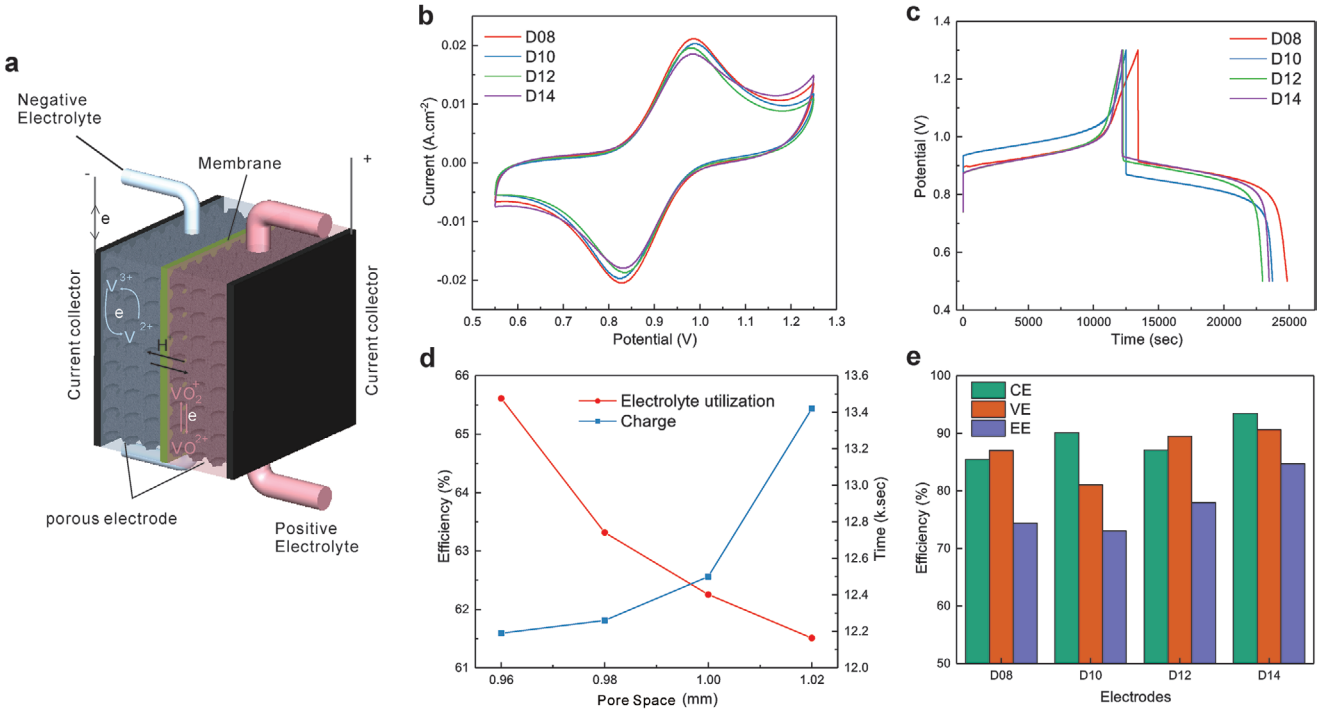


Figure 7. The printed electrodes utilized in the vanadium redox flow battery. a) Schematic diagram of vanadium redox flow battery representing the dynamic EES system; b) CV curves of electrodes with different pore spaces (D00 series electrodes in Table S4, Supporting Information) at a 1.1 mm designed diameter in $VOSO_4$ (0.1 M) supported in H_2SO_4 (3 M) at 5 mV s^{-1}; c) galvanostatic charge–discharge curves of D00 series electrodes in $VOSO_4$ (0.1 M) supported in H_2SO_4 (3 M) electrolyte at a current densities of 10 mA cm^{-2} from 0.5 to 1.3 V; d) electrolyte utilization ratio and charge time of D00 series electrodes; e) the Coulombic efficiency (CE), voltage efficiency (VE), and energy efficiency (EE) of the VRFBs with D00 series electrodes at 10 mA cm^{-2} current densities.

© 2020 The Authors. Published by WILEY-VCH Verlag GmbH & Co. KGaA, Weinheim

raising until the minimum SSA sample (S25, Table S4, Supporting Information). Meanwhile, the galvanostatic charge–discharge curves (Figure 6c) show a decrease against the charge/discharge time. It should be noticed from Figure 6d that the specific capacitances of S25 (12.89 F g^{-1}) are much lower than S20 (17.93 F g^{-1}) despite nearly the same SSA, porosity and resistance (Table S4, Supporting Information). This is because the effective diffusivity of K^+ in S25 electrode is higher than the S20 (Table S4, Supporting Information). As shown in Figure 6e, the S10 electrode presents the largest capacitances (38.45 F g^{-1}) since the large specific surface area and small wall thickness among the electrodes (Table S4, Supporting Information). However, the specific capacitances (30–40 F g^{-1}) is lower compared with the other carbon supercapacitors,[7,16,28] due to the activation conditions should be further optimized comprehensively considering the activation temperature, activation time, and activator amount for high performance.

The application of the vanadium redox flow battery is depicted in Figure 7a. In the cell design, the electrolyte flow through the designed macro-architectures to ensure the electrodes are immersed. Subsequently, the electrolyte with active species (VO^{2+}/VO_2^+ in this half-cell test) are conveyed into the inner carbon matrix through macropores. Then the active species transport by mesopores to the active site, followed by the redox reaction. The electrons migrate through the external circuit and drive the loading. Similar values of ΔE_p (Figure 7b) in the CV test imply close electrocatalytic performance. The slightly higher PCD of D08 can be attributed to the maximum SSA and minimum resistance (Table S4, Supporting Information). On the contrary, the D14 shows the lowest PCD is because of the maximum resistance and minimum SSA. The charge time and electrolyte utilization of the positive electrode in an H-type cell were presented in Figure 7c,d, respectively. The D14 electrode exhibit the maximum electrolyte utilization ratio (65.6%) and the least charge time (12 190 s). It is because of the superior diffusion performance in the carbon matrix resulting from the minimum thickness and maximum porosity (Table S4, Supporting Information). However, the electrolyte utilization ratio is smaller than Zhengyang's work (72%)[20] and Zhou's work (58–92%),[62] since the leakage of the H-type cell. As Figure 7e shown, the D14 electrode exhibits the excellent coulombic efficiency (93.48%), voltage efficiency (90.64%), and energy efficiency (84.73%) than the other electrodes, benefiting from the superior ion transport performance. The energy efficiency is comparable with the other researchers' works,[20,56,63,64] considering the quite small current density, the low concentration of active species, and the electrolyte leakage in the H-type cell. This phenomenon confirms the mass transport plays a crucial role in the flow battery, when the specific surface area, resistance, and electrocatalytic ability are similar.

3. Conclusion

A novel hybrid manufacturing method to fabricate 3D hierarchical porous carbon electrodes for electrochemical energy storage is developed. The electrode structure was printed through SLA to manufacture the bespoke macro-architectures at the micrometer scale, followed by a slow pyrolysis process to carbonize the electrode structure. At last, an activation process was implemented to enrich the micro-, meso-, and macropores of the carbon. The hybrid manufacturing has enabled the fabrication of hierarchical porous structures in the scale range from nanometer to micrometer to maximize the electrochemical performance. The process has been proven an efficient approach to develop highly electro-active electrodes, with 5.85-fold greater PCD than the commercial carbon papers in the ferri/ferro system. The porosity and SSA of the carbon electrode can be facilely manipulated by adjusting the hole diameter and overlap ratio, which provides great opportunities on tuning electrode structure for a specific application scenario. It can be concluded that small designed hole diameter in the macro-architecture can enhance both effective diffusivity and SSA, while a low overlap ratio improves the SSA and electroconductivity, but restrains the effective diffusivity. The 3D carbon electrodes were applied in two energy storage systems, that is, supercapacitor and VRFB. In both systems, the SSA was found the most crucial element to determine electrochemical performance. In VRFB, maintaining high effective diffusivity of reactant in pore structure is more important than reducing the electrical resistance. The novel hybrid manufacture method, along with the improved understanding of the structure-performance relationship, paves a new way to fabricate carbon electrodes. After materials and structure optimization, the electrodes with high electrocatalytic performance, larger surface area, small ohmic resistance, and even the low pressure drop in the flow cells, can be obtained.

4. Experimental Section

Carbon Structure Manufacture: All the models were designed by SolidWorks 2014 (Dassault Systemes S.A.) and printed on an SLA machine (RS6000, UnionTech) using a commercial photosensitive resin (SOMOS IMAGINE 8000, DSM, Holland). These designs are shown in Figure S6, Supporting Information, containing three series: C10 electrode with cubic pores; D00 series for the electrodes with different pore spaces named D06, D08, D10, D12, and D14; and S00 electrodes with different spherical pore diameters named S10, S15, S20, S25, and S30. After washed and dried (Figure S7, Supporting Information), the structures were heated in a quartz tube furnace filled with high purity nitrogen (99.999 vol%) at 760, 860, and 960 °C (Table S3, Supporting Information) for 4 h at 101.3 kPa. To exclude the influences from water steam and oxygen, all the devices in the furnace (furnace plugs, crucibles, and flanges) were dried at 120 °C and high purity nitrogen (99.999 vol%). The optical and SEM images of these pyrolyzed carbon structures are seen in Figures S8 and S1, Supporting Information, respectively. Finally, the steam or KOH activation was conducted in a N_2 flow (200 mL min^{-1}). The temperatures were 700 and 800 °C for steam and KOH activation, respectively, and KOH was added into the carbon electrode in both approaches (seen in Supporting Methods, Supporting Information). The detailed activation parameters are listed in Table S3, Supporting Information.

Materials Characterization: The TGA was conducted on NETZSCH STA 409 PC/PG analyzer in high purity nitrogen at 5 °C min^{-1} heating rate at 101.3 kPa to determine the main mass loss region of the additive manufactured resin. SEM images were obtained on HITACHI S-3400N machine equipped a CDU X-ray detector and a digital pulse height analyzer, which could detect the elements from the fifth one (B) to the 92nd one (U). FESEM experiments were performed on GeminiSEM 500 electron microscopes. High-resolution transmission electron microscopy images were acquired from an FEI Tecnai G2 F20

© 2020 The Authors. Published by WILEY-VCH Verlag GmbH & Co. KGaA, Weinheim

microscope with an operating voltage of 200 kV. The XRD measurements were carried out on a D/max2550VB/PC X-ray diffractometer. The 2θ angular region was between 5° and 80°. Raman spectra were acquired from an inVia Reflex Laser Micro-Raman Spectrometer with 514 nm laser excitation. N_2 adsorption–desorption analysis was carried out on a Micrometrics ASAP 2020 to analyze the porosity and pore size distribution. The carbon samples were degassed under vacuum at 150 °C for 12 h, and all adsorption–desorption measurements were carried out at –196 °C. The functional groups on designed carbon were detected by Fourier transform infrared spectra (FTIR, Nicolet 6700).

Electrochemical Measurements: All the electrochemical measurements were carried out on CHI660E electrochemical workstation. The techniques utilized for different electrodes were listed in Table S3, Supporting Information. The CV, chronoamperometry (CA), and GCD measurements were conducted in a conventional three-electrode cell at room temperature. All the printed electrodes were utilized as a working electrode, a platinum plate electrode (1 cm^2) was employed as the counter electrode, and the Ag/AgCl electrode (in 3.5 M KCl) was acted as a reference electrode. Before the collection of the final date, more than 50 cycles of CV test were conducted until the curves were stable to ensure the stability of the materials (Figure S9, Supporting Information). For the investigation of the macropores effect, the electrolyte consisting of $K_3Fe(CN)_6$ (1 mM) and KCl (0.5 M) solution was employed. The CV was performed from –0.1 to 0.6 V, CA was conducted under the initial potential of 0.6 V, and EIS was carried out at 0.25 V with the excitation signal of 5 mV in the frequency range from 10^5 to 10^{-1} Hz. For the supercapacitor application, the KOH solution (6 M) was selected as the electrolyte, while C10 and S00 electrodes were involved. The CV (–1.0 to 0 V), and GCD measurements were performed for the S00 and C10 electrodes. The CV (0.55–1.25 V), EIS (potential: 0.91 V, amplitude: 5 mV, frequency: 10^5 to 10^{-1} Hz) were performed in $VOSO_4$ (0.1 M) and H_2SO_4 (3 M) solution for VRFB applications on D00 and C10 electrodes. An H-type glass cell was employed for the VRFB application. Each compartment contained 15 mL electrolytes with a magnetic stirrer. The electrolytes were separated by quartz sands. The working electrode and reference electrode were placed on the side with $VOSO_4$ (0.1 M) and H_2SO_4 (3 M) solution, and the counter electrode was placed on the other side with H_2SO_4 (3 M). The cell test was performed at current densities of 10 mA cm^{-2} with the potential range from 1.25 to 0.55 V.

Supporting Information

Supporting Information is available from the Wiley Online Library or from the author.

Acknowledgements

This work was supported by the National Natural Science Foundation of China (No. 51776074), the Royal Society under grant number RSG\R1\180162, and the UK Engineering and Physical Sciences Research Council under grant number EP/R012164/2.

Conflict of Interest

The authors declare no conflict of interest.

Keywords

additive manufacturing, controllable structures, electrochemical energy storages, hierarchical porous carbon, structure–performance relations

Received: November 18, 2019
Revised: March 26, 2020
Published online: April 27, 2020

[1] E. S. Beh, D. de Porcellinis, R. L. Gracia, K. T. Xia, R. G. Gordon, M. J. Aziz, *ACS Energy Lett.* **2017**, *2*, 639.
[2] X. Jin, J. Wu, Y. Mu, M. Wang, X. Xu, H. Jia, *Appl. Energy* **2017**, *208*, 480.
[3] L.-F. Chen, Y. Feng, H.-W. Liang, Z.-Y. Wu, S.-H. Yu, *Adv. Energy Mater.* **2017**, *7*, 1700826.
[4] H. Zhang, H. T. Chung, D. A. Cullen, S. Wagner, U. I. Kramm, K. L. More, P. Zelenay, G. Wu, *Energy Environ. Sci.* **2019**, *12*, 2548.
[5] Z. Sun, J. Zhang, L. Yin, G. Hu, R. Fang, H.-M. Cheng, F. Li, *Nat. Commun.* **2017**, *8*, 14627.
[6] Q. Zheng, F. Xing, X. Li, G. Ning, H. Zhang, *J. Power Sources* **2016**, *324*, 402.
[7] D. Jia, X. Yu, H. Tan, X. Li, F. Han, L. Li, H. Liu, *J. Mater. Chem. A* **2017**, *5*, 1516.
[8] S. Dutta, A. Bhaumik, K. C. W. Wu, *Energy Environ. Sci.* **2014**, *7*, 3574.
[9] Y.-P. Gao, Z.-B. Zhai, K.-J. Huang, Y.-Y. Zhang, *New J. Chem.* **2017**, *41*, 11456.
[10] P. Hao, Z. Zhao, J. Tian, H. Li, Y. Sang, G. Yu, H. Cai, H. Liu, C. P. Wong, A. Umar, *Nanoscale* **2014**, *6*, 12120.
[11] B. Lee, C. Lee, T. Liu, K. Eom, Z. Chen, S. Noda, T. F. Fuller, H. D. Jang, S. W. Lee, *Nanoscale* **2016**, *8*, 12330.
[12] J. H. Um, M. Choi, H. Park, Y. H. Cho, D. C. Dunand, H. Choe, Y. E. Sung, *Sci. Rep.* **2016**, *6*, 18626.
[13] N. Guo, M. C. Leu, U. O. Koylu, *Int. J. Hydrogen Energy* **2014**, *39*, 21185.
[14] J. Marschewski, L. Brenner, N. Ebejer, P. Ruch, B. Michel, D. Poulikakos, *Energy Environ. Sci.* **2017**, *10*, 780.
[15] H. Feng, H. Hu, H. Dong, Y. Xiao, Y. Cai, B. Lei, Y. Liu, M. Zheng, *J. Power Sources* **2016**, *302*, 164.
[16] S. H. Du, L. Q. Wang, X. T. Fu, M. M. Chen, C. Y. Wang, *Bioresour. Technol.* **2013**, *139*, 406.
[17] J. Liu, Z. A. Wang, X. W. Wu, X. H. Yuan, J. P. Hu, Q. M. Zhou, Z. H. Liu, Y. P. Wu, *J. Power Sources* **2015**, *299*, 301.
[18] L. Estevez, R. Dua, N. Bhandari, A. Ramanujapuram, P. Wang, E. P. Giannelis, *Energy Environ. Sci.* **2013**, *6*, 1785.
[19] X. L. Zhou, Y. K. Zeng, X. B. Zhu, L. Wei, T. S. Zhao, *J. Power Sources* **2016**, *325*, 329.
[20] Z. Zhang, J. Xi, H. Zhou, X. Qiu, *Electrochim. Acta* **2016**, *218*, 15.
[21] Y. V. Kaneti, S. Dutta, M. S. A. Hossain, M. J. A. Shiddiky, K. L. Tung, F. K. Shieh, C. K. Tsung, K. C. Wu, Y. Yamauchi, *Adv. Mater.* **2017**, *29*, 1700213.
[22] C.-H. Huang, R.-A. Doong, *Microporous Mesoporous Mater.* **2012**, *147*, 47.
[23] S. Chen, G. He, H. Hu, S. Jin, Y. Zhou, Y. He, S. He, F. Zhao, H. Hou, *Energy Environ. Sci.* **2013**, *6*, 2435.
[24] A. Azhar, Y. Li, Z. Cai, M. B. Zakaria, M. K. Masud, M. S. A. Hossain, J. Kim, W. Zhang, J. Na, Y. Yamauchi, M. Hu, *Bull. Chem. Soc. Jpn.* **2019**, *92*, 875.
[25] J. Wang, P. Nie, B. Ding, S. Dong, X. Hao, H. Dou, X. Zhang, *J. Mater. Chem. A* **2017**, *5*, 2411.
[26] K. Xu, A. Loh, B. Wang, X. Li, *J. Electrochem. Soc.* **2018**, *165*, A809.
[27] X. Fan, S. Li, L. Lu, *Electrochim. Acta* **2016**, *200*, 152.
[28] C. Zhu, T. Liu, F. Qian, T. Y. Han, E. B. Duoss, J. D. Kuntz, C. M. Spadaccini, M. A. Worsley, Y. Li, *Nano Lett.* **2016**, *16*, 3448.
[29] C. Zhu, T. Y. Han, E. B. Duoss, A. M. Golobic, J. D. Kuntz, C. M. Spadaccini, M. A. Worsley, *Nat. Commun.* **2015**, *6*, 6962.
[30] X. Wei, D. Li, W. Jiang, Z. Gu, X. Wang, Z. Zhang, Z. Sun, *Sci. Rep.* **2015**, *5*, 11181.
[31] C. W. Foster, M. P. Down, Y. Zhang, X. Ji, S. J. Rowleyneale, G. C. Smith, P. J. Kelly, C. E. Banks, *Sci. Rep.* **2017**, *7*, 42233.
[32] A. Azhari, E. Marzbanrad, D. Yilman, E. Toyserkani, M. A. Pope, *Carbon* **2017**, *119*, 257.
[33] X. Yi, Z.-J. Tan, W.-J. Yu, J. Li, B.-J. Li, B.-Y. Huang, J. Liao, *Carbon* **2016**, *96*, 603.

© 2020 The Authors. Published by WILEY-VCH Verlag GmbH & Co. KGaA, Weinheim

[34] J. Bauer, A. Schroer, R. Schwaiger, O. Kraft, *Nat. Mater.* **2016**, *15*, 438.
[35] X. Chen, G. Zhao, Y. Wu, Y. Huang, Y. Liu, J. He, L. Wang, Q. Lian, D. Li, *Carbon* **2017**, *123*, 34.
[36] B. Bian, D. Shi, X. Cai, M. Hu, Q. Guo, C. Zhang, Q. Wang, A. X. Sun, J. Yang, *Nano Energy* **2018**, *44*, 174.
[37] C. Yang, Q. Cao, P. Puthongkham, S. T. Lee, M. Ganesana, N. V. Lavrik, B. J. Venton, *Angew. Chem., Int. Ed.* **2018**, *57*, 14255.
[38] P. Tian, C. Chen, J. Hu, J. Qi, Q. Wang, J. C. Chen, J. Cavanaugh, Y. Peng, M. M. Cheng, *Biomed. Microdevices* **2018**, *20*, 4.
[39] J. Wang, P. Nie, B. Ding, S. Dong, X. Hao, H. Dou, X. Zhang, *J. Mater. Chem. A* **2016**, *5*, 2411.
[40] C. Ma, Z. Ma, L. Gao, Y. Liu, T. Wu, F. Wang, H. Ishida, *Mater. Des.* **2019**, *180*, 107954.
[41] A. M. Rahmatika, W. Yuan, A. F. Arif, R. Balgis, K. Miyajima, G. M. Anilkumar, K. Okuyama, T. Ogi, *Ind. Eng. Chem. Res.* **2018**, *57*, 11335.
[42] D. Zhang, C. He, J. Zhao, J. Wang, K. Li, *J. Colloid Interface Sci.* **2019**, *546*, 101.
[43] A. F. Arif, Y. Chikuchi, R. Balgis, T. Ogi, K. Okuyama, *RSC Adv.* **2016**, *6*, 83421.
[44] R. Balgis, T. Ogi, A. F. Arif, G. M. Anilkumar, T. Mori, K. Okuyama, *Carbon* **2015**, *84*, 281.
[45] J. Wang, J. Tang, B. Ding, V. Malgras, Z. Chang, X. Hao, Y. Wang, H. Dou, X. Zhang, Y. Yamauchi, *Nat. Commun.* **2017**, *8*, 15717.
[46] H. Xuan, Y. Wang, G. Lin, F. Wang, L. Zhou, X. Dong, Z. Chen, *RSC Adv.* **2016**, *6*, 15313.
[47] Z. Zhang, J. Zhang, X. Zhao, F. Yang, *Carbon* **2015**, *95*, 552.
[48] A. C. Ferrari, J. C. Meyer, V. Scardaci, C. Casiraghi, M. Lazzeri, F. Mauri, S. Piscanec, D. Jiang, K. S. Novoselov, S. Roth, A. K. Geim, *Phys. Rev. Lett.* **2006**, *97*, 187401.
[49] L. Dai, Y. Jiang, W. Meng, H. Zhou, L. Wang, Z. He, *Appl. Surf. Sci.* **2017**, *401*, 106.
[50] M. Ulaganathan, A. Jain, V. Aravindan, S. Jayaraman, W. C. Ling, T. M. Lim, M. P. Srinivasan, Q. Yan, S. Madhavi, *J. Power Sources* **2015**, *274*, 846.
[51] T. Liu, X. Li, C. Xu, H. Zhang, *ACS Appl. Mater. Interfaces* **2017**, *9*, 4626.
[52] W. Ao, J. Fu, X. Mao, Q. Kang, C. Ran, Y. Liu, H. Zhang, Z. Gao, J. Li, G. Liu, J. Dai, *Renewable Sustainable Energy Rev.* **2018**, *92*, 958.
[53] A. M. Abioye, F. N. Ani, *Renewable Sustainable Energy Rev.* **2015**, *52*, 1282.
[54] S. De, A. M. Balu, J. C. van der Waal, R. Luque, *ChemCatChem* **2015**, *7*, 1608.
[55] J. S. Cha, S. H. Park, S.-C. Jung, C. Ryu, J.-K. Jeon, M.-C. Shin, Y.-K. Park, *J. Ind. Eng. Chem.* **2016**, *40*, 1.
[56] D. M. Kabtamu, J.-Y. Chen, Y.-C. Chang, C.-H. Wang, *J. Power Sources* **2017**, *341*, 270.
[57] Q. Wang, Z. G. Qu, Z. Y. Jiang, W. W. Yang, *Appl. Energy* **2018**, *220*, 106.
[58] Q. Wang, Z. G. Qu, Z. Y. Jiang, W. W. Yang, *Appl. Energy* **2018**, *213*, 293.
[59] K. Hamamoto, M. Fukushima, M. Mamiya, Y. Yoshizawa, J. Akimoto, T. Suzuki, Y. Fujishiro, *Solid State Ionics* **2012**, *225*, 560.
[60] L. Zhao, J. Li, F. Battaglia, Z. He, *J. Power Sources* **2016**, *333*, 83.
[61] J. Li, J. Li, H. Feng, Y. Zhang, J. Jiang, Y. Feng, M. Chen, D. Qian, *Electrochim. Acta* **2015**, *153*, 352.
[62] X. L. Zhou, T. S. Zhao, Y. K. Zeng, L. An, L. Wei, *J. Power Sources* **2016**, *329*, 247.
[63] J. Kim, H. Lim, J.-Y. Jyoung, E.-S. Lee, J. S. Yi, D. Lee, *Carbon* **2017**, *111*, 592.
[64] C. Zhao, Y. Li, Z. He, Y. Jiang, L. Li, F. Jiang, H. Zhou, J. Zhu, W. Meng, L. Wang, L. Dai, *J. Energy Chem.* **2019**, *29*, 103.

© 2020 The Authors. Published by WILEY-VCH Verlag GmbH & Co. KGaA, Weinheim